CHEMISTRY OF MATERIALS

Article

pubs.acs.org/cm

Bismuth Iridium Oxide Oxygen Evolution Catalyst from Hydrothermal Synthesis

Kripasindhu Sardar,[†,‡] Sarah C. Ball,[‡] Jonathan D.B. Sharman,[‡] David Thompsett,[‡] Janet M. Fisher,[‡] Richard A.P. Smith,[†] Pabitra K. Biswas,[§] Martin R. Lees,[§] Reza J. Kashtiban,[§] Jeremy Sloan,[§] and Richard I. Walton*[,†]

[†]Department of Chemistry, University of Warwick, Coventry, CV4 7AL, United Kingdom

[‡]Johnson Matthey Technology Centre, Sonning Common, Reading, RG4 9NH, United Kingdom

[§]Department of Physics, University of Warwick, Coventry, CV4 7AL, United Kingdom

ABSTRACT: We present a detailed characterization of the pyrochlore $Bi_2Ir_2O_7$ prepared by a one-step hydrothermal synthesis route from aqueous sodium hydroxide solution of $NaBiO_3{\cdot}2H_2O$ and $IrCl_3{\cdot}5H_2O$ in the presence of Na_2O_2 at 240 °C. Using 5 M NaOH solution as the reaction medium, a fine powder of polycrystalline $Bi_2Ir_2O_7$ with an average crystal size of 10 nm and surface area of ~46 $m^2\ g^{-1}$ is produced. Structure refinement against powder neutron diffraction reveals a stoichiometric pyrochlore with no evidence for significant oxide-ion defects. X-ray absorption near-edge structure (XANES) spectra recorded at both metal L_{III}-edges show that, although Bi is present solely as Bi^{3+}, there is evidence for the oxidation of iridium slightly beyond +4. This would suggest some surface oxidation of iridium, which is also shown by X-ray photoelectron spectroscopy (XPS) measurements. Magnetization data, as a function of temperature, show that the system is paramagnetic down to a temperature of 2 K, while the electrical conductivity shows hydrothermal $Bi_2Ir_2O_7$ to be a metallic conductor. In electrochemical tests, performed on rotating disk electrodes fabricated from the powdered iridate and Nafion solution, the material shows oxygen evolution activity in acidic solution, comparable to the most active precious-metal oxide materials, with reproducibility over >1000 cycles, demonstrating the formation of robust electrodes.

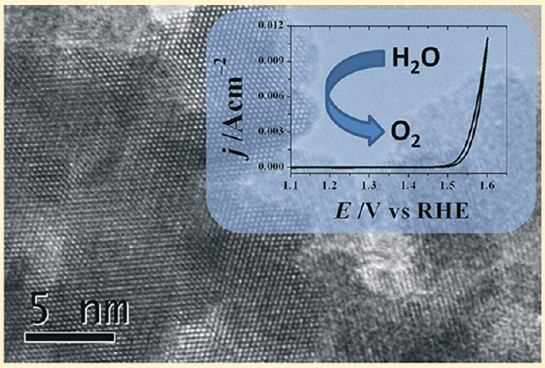

KEYWORDS: *pyrochlore, neutron diffraction, electrocatalysis, oxygen evolution, XANES*

INTRODUCTION

Catalysts of the oxygen evolution reaction (OER) and oxygen reduction reaction (ORR) in aqueous media (both acidic and basic) are highly desirable for applications concerning energy production and storage, such as use in batteries, electrolyzers, and fuel cells.[1] A good example is in proton exchange membrane (PEM) electrolyzers, which are being developed to replace traditional alkaline electrolyzers.[2] For such devices, water electrolysis requires highly active oxygen evolving anodes and some of the most active electrocatalysts are established to be oxides of the precious metals ruthenium and iridium.[3] Particular focus has been on mixed oxides such as $Ru_{1-x}Ir_xO_2$[4−7] and IrO_2−Ta_2O_5.[4,8] For these materials, however, the materials actually used may show significant local inhomogeneity within crystallites, such as surface segregation of one metal,[7] or actually be poorly defined mixtures rather than true single phases.[9] For application, an electrocatalyst material must show high activity at accessible potentials but also maintain activity over many cycles. While it is established that both Ru and Ir have stable +4 and +5 oxidation states, which feasibly may be interconverted to allow activation of water at the catalyst surface, there has been much speculation as to the mode of operation of the precious-metal oxides as electrocatalysts, with no real consensus reached in the literature. For example, some consider it may be possible that a link between electrochemical activity and band structure of the solid exists,[10] or that the metal−oxygen binding energy plays a role in determining activity,[3,11] and for complex, mixed-metal oxides, the presence of oxygen vacancies may be important.[12] In reality, of course, an interplay of these factors may be at play.

The most-detailed model proposed for the OER at complex mixed-metal iridium oxide materials was presented by Goodenough and co-workers.[12] They suggested that, for the oxide $Pb_2(Pb,Ir)_2O_{7-\delta}$, the displacement of surface hydroxide ions linked to Pb by superoxide anions maintains the octahedral coordination but allows oxygen evolution, mediated by the Ir^{4+}/Ir^{5+} couple via exchange of surface O^- species.[12] Later, ten Kortenaar et al. studied a variety of mixed-metal iridium oxides containing iridium in different oxidation states and encompassing a range of structure types, and while all showed some

Received: August 3, 2012
Revised: October 10, 2012
Published: October 10, 2012

activity toward the ORR and the OER, no correlation between electrochemical and electronic properties could be found.[13] Recent work in this field has examined nanocrystalline iridium oxides and suggested oxidation to the +VI state may occur during electrochemistry,[14] while Lyons and Floquet presented extensive experimental evidence for the role of surface aqua groups in oxygen evolution, and also high oxidation states of Ru and Ir (+VII and +VI, respectively) were implicated.[6]

The surface properties of materials for electrocatalysis are crucial for dictating and, potentially, controlling their activity. On a more practical level, fine powders of electrocatalysis for ease of fabrication of electrodes are highly desirable. In the synthesis of complex, mixed-metal oxide materials, high-temperature solid-state synthesis limits any fine control of crystal size; hence, soft chemical approaches for the preparation of oxide powders must be developed. Indeed, for some of the ruthenate and iridate materials mentioned above, sol–gel approaches have been used to permit homogenization of metal precursors before a gentle annealing is used to bring about crystallization.[15] A further consideration in the synthesis of ruthenium and iridium oxides is the ease with which the metals are reduced to the elemental, metallic state: this must be avoided, using carefully controlled oxidizing conditions.

Hydrothermal synthesis, where metal salts are dissolved in water under acidic or basic conditions (with the addition of oxidants or reductants) and heated above 100 °C in a sealed reaction vessel, offers an attractive route to mixed-oxide materials, where control of the crystallite size and the metal oxidation state may be possible.[16] Following from our recent work on the subcritical hydrothermal synthesis of some alkali-earth iridium oxides and hydroxides[17] and of a ruthenate pyrochlore oxide,[18] we have turned our attention to using the method for the preparation of pyrochlore-type bismuth–iridium oxides that may have desirable electrocatalytic properties. Our approach to synthesis has been to use the combination of the bismuth(V) salt $NaBiO_3{\cdot}2H_2O$ as an oxidant and the salt $Ir^{III}Cl_3{\cdot}5H_2O$ as a soluble iridium source to enable the isolation of a mixed oxide containing iridium in a higher oxidation state; this is based on a similar approach that has successfully been used in the hydrothermal formation of other mixed-metal bismuth oxides, including those containing cerium[19] and manganese.[20]

EXPERIMENTAL SECTION

1. Synthesis. Stoichiometric amounts of $NaBiO_3{\cdot}2H_2O$ (Sigma–Aldrich, >80%) and $IrCl_3{\cdot}5H_2O$ (Alfa–Aesar, 52.77 wt % Ir) in a 1:1 molar ratio (the water content of the metal salts was determined accurately using thermogravimetric analysis (TGA) before use) using accurately weighed ∼0.6 mmol of sodium bismuthate were added to a Teflon-lined 23-mL autoclave, followed by the addition of 8 mL of NaOH solution (either 5 or 12 M, see below). The resulting suspension was stirred for 3 h after which solid Na_2O_2 (8 mol equiv, with respect to iridium) was added. In exploratory hydrothermal reactions, we found that the presence of an additional oxidant was crucial for the formation of oxides with higher oxidation states of iridium, and in the absence of this additional oxidant, Ir metal and other unidentified phases could not be avoided in the products. Na_2O_2 is a convenient to use, solid oxidant that avoids the use of liquid H_2O_2. The autoclave was sealed immediately and then placed inside a preheated fan oven and maintained at 240 °C for 120 h. The autoclaves were cooled to room temperature, the solid product was recovered by suction filtration, washed with deionized water, and dried in air at 100 °C.

2. Laboratory Characterization. Transmission electron microscopy (TEM) was performed using a JEOL Model 2100 LaB_6 instrument, operating at 200 kV. The specimens were dispersed ultrasonically in ethanol and then deposited dropwise onto 3-mm lacey carbon grids supplied by Agar. Energy-dispersive X-ray analysis (EDXA) was performed using the TEM system with an Oxford Instruments X-max silicon drift detector (SDD) with a large 80 mm^2 active area and INCA X-ray microanalysis software. Powder X-ray diffraction (XRD) data were collected using Bruker D8 Advance X-ray diffractometer operating with Cu Kα radiation and equipped with a VÅNTEC-1 solid-state detector. Thermogravimetric analysis (TGA) was carried out using a Mettler Toledo instrument with a heating rate of 10 °C/min, under a flow of nitrogen. ICP analysis for metals was performed by Medac, Ltd. (U.K.) using ICP-OES for metals after digestion of solid samples in HBr. BET surface area was measured using Micromeritics Tristar3000 with degassing at 200 °C for 15 h under N_2 flow and data taken from a seven-point linear fit between the P/P_0 range of 0.05–0.20. X-ray photoelectron spectroscopy (XPS) was performed using a Thermo Escalab 250 system. The radiation used was monochromatized Al Kα radiation with a 650 μm spot size. Charge compensation was provided by the in-lens electron flood gun at a 2-eV setting and the "401" unit for "zero energy" Ar ions.

The magnetization of the samples was measured in the temperature range of 400–2 K using a Quantum Design Magnetic Property Measurement System SQUID magnetometer. Both zero-field-cooled warming and field-cooled cooling magnetization (M) data, versus temperature, were recorded with applied magnetic fields of either 100 or 10000 Oersteds. Magnetization versus applied field (H) was studied at 2 K. To measure the resistivity of samples, as-prepared powders were pressed into circular disks and sintered at 750 °C for 24 h in air. A conventional four probe technique was employed using a Quantum Design Physical Property Measurement System.

3. Neutron Diffraction. Powder neutron diffraction experiments studies were made of one of the crystalline samples of bismuth iridate prepared (see below) using the instrument GEM[21] at ISIS, the UK spallation neutron source. The sample was loaded into a vanadium can with an inner diameter of 7.62 mm and data were accumulated for ∼ 5 h to ensure they were of good statistical quality. Data were also collected from an empty vanadium can, the empty instrument, and a vanadium rod, for normalization purposes. Three banks of data from GEM were analyzed simultaneously using the GSAS suite of software,[22] visualized with EXPGUI.[23]

4. X-ray Absorption Near Edge Structure Spectroscopy (XANES). XANES experiments were performed using beamline B18 of the Diamond Light Source, U.K.[24] This beamline provides X-ray energies in the range of 2.05–35 keV, using a fixed-exit, double-crystal Si(111) monochromator, which provided an energy resolution of 2×10^4. The optics of the beamline include a collimating mirror and a toroidal focusing mirror before and after the monochromator, respectively and the measurements were carried out using the Cr coating of these two optical elements. Under this configuration, the expected flux on the sample is of the order of 5×10^{11} photons s^{-1} and the size of the beam at that position is ∼200 μm in the vertical direction by 150 μm in the horizontal one. In our experiments, small samples (∼20 mg) of materials to be studied were ground finely with polyethylene powder (∼ 80 mg) under acetone and after evaporation of the solvent pressed into 13-mm-diameter pellets of ∼1 mm thickness under a pressure of 5 Tonnes. XANES data were collected at the Bi L_{III} and Ir L_{III} edges in transmission mode with ion chambers before and behind the sample filled with appropriate mixtures of inert gases to optimize sensitivity. The spectra were measured with a step size equivalent to <0.5 eV. Data were normalized using the program Athena[25] with a linear pre-edge and polynomial post-edge background subtracted from the raw $\ln(I_t/I_0)$ data.

5. Electrochemistry. To fabricate electrodes, a typical ink preparation was as follows: to 60 mg $Bi_2Ir_2O_7$, 2.2 mL of isopropanol, 8.8 mL of deionized (DI) water, and 432 μL of 6.43% aqueous Nafion solution was added. The entire mixture was homogenized by a high-power sonication probe operating at 6 W for 10 min. Fifteen microliters (15 μL) of the ink prepared as described above was dispensed onto the gold disk of a rotating disk electrode (RDE, Pine Instrument, 0.196 cm^2) and then dried in air under a lamp at 110 °C

dx.doi.org/10.1021/cm302468b | Chem. Mater. 2012, 24, 4192–4200

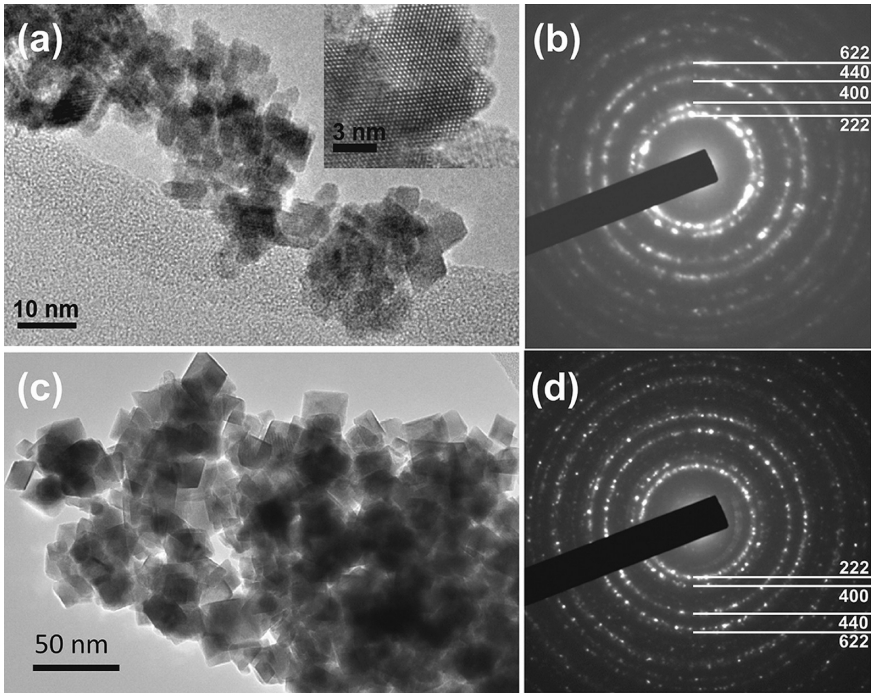

Figure 1. (a, c) TEM and (b, d) SAED images of bismuth iridium oxide prepared in (a, b) 5 M NaOH solution and (c, d) 12 M NaOH solution.

for 2 h. This gave a catalyst loading of 402 $\mu g/cm^2$ geometric on the RDE. For each electrochemical experiment, a fresh electrode with similar catalyst loading was fabricated in the same way. A conventional three-electrode electrochemical cell was used for all the electrochemical measurements. The electrolyte 1 M H_2SO_4 was saturated with nitrogen by bubbling N_2 gas through the solution for 1 h before measurements. The working electrode was a thin layer of catalyst prepared on RDE as described above; the reference electrode was a standard reversible hydrogen electrode (RHE), and the counter electrode was a Pt wire. The electrochemical experiments were all performed at room temperature (25 °C). Typically, the first cyclic voltammogram was recorded between 0.02−1.5 V with different sweep rates within the range of 1−400 mV s^{-1}, followed by measurement of the activity of oxygen evolution reaction by recording a cyclic voltammogram over 1.0−1.6 V at a sweep rate of 1 mV s^{-1}. To assess stability, repetitive cyclic voltammetry (CV) was performed between 0.02 V and 1.5 V for up to 1000 cycles at 50 mV s^{-1}; after each 50 cycles, a cyclic voltammogram was recorded at a sweep rate of 10 and 50 mV s^{-1} for surface characterization, and 1 mV s^{-1} for the determination of OER activity. During the entire measurement, the RDE was rotated at 900 rpm while N_2 gas was purged continuously through the electrolyte solution. In order to correct the potential due to the ohmic resistance drop of the solution, the resistance of each solution was measured using an ac impedance method.

■ RESULTS AND DISCUSSION

Figure 1 shows TEM of materials prepared using 5 and 12 M NaOH solution. This illustrates a pH dependence of the crystallite size of the material formed. The average crystallite sizes obtained from the Scherrer analysis of powder XRD patterns were 10 and 26 nm for samples prepared with 5 and 12 M NaOH solution, respectively, consistent with the TEM observations. The BET surface areas of these samples were measured as 46 and 21 m^2 g^{-1}, respectively, reflecting the differences in average crystallite size. EDXA showed both samples to contain close to a 1:1 ratio of Bi:Ir (typical analysis of 20 crystals gave a ratio of 1:0.92), and bulk analysis for metals using ICP gave a Bi:Ir ratio of 1:1.01. Despite the small particle size, the particles formed are of high crystallinity (as shown by the SAED images; Figure 1).

Powder XRD analysis indicated the formation of a face-centered cubic (fcc) pyrochlore type material and a composition $Bi_2Ir_2O_7$ is therefore consistent with the EDXA analysis and also bulk analysis for metals. Neutron diffraction analysis was performed to allow an accurate refinement of the oxygen content of the material, since it is well-known that pyrochlore materials may contain oxygen excess, oxygen deficiency, or other structural defects resulting from oxide-ion displacement from their ideal positions.[26] The sample studied by neutron diffraction was that prepared using 5 M NaOH, since the smaller crystallite size of this specimen made it more appropriate for the electrochemical characterization described below. The crystal structure of a stoichiometric $A_2B_2O_7$ pyrochlore provided the starting point for structure refinement with Bi on the distorted eight-coordinate A-site and iridium on the six-coordinate B-site. Neutron diffraction data from Banks 4, 5, and 6 of the GEM diffractometer (these have average scattering angle ranges of 50°−74°, 79°−105°, and 142°−170°, respectively) were simultaneously refined against to maximize the number of data points and obtain the most accurate structure model. The simple pyrochlore model gave a satisfactory fit to the observed data (Figure 2), with physically reasonable isotropic values for temperature factors. There is no evidence of any lower symmetry, that may be seen in defect pyrochlores.[27] In our refined model (Table 1), the *x*-coordinate of the 48*f* oxygen of 0.32629(13) falls within the expected range for the pyrochlore structure.[26] Refinement of site occupancies of Bi and the 8b O gave little deviation from the stoichiometric composition (this resulted in a refined composition $Bi_{1.96}Ir_2O_{6.92}$) and only a small improvement in fit parameters. Given that both iridium and bismuth may adopt more than one oxidation state, the possibility of the inclusion of excess oxygen in the form of oxide anions on the otherwise unoccupied 8a site was investigated, as seen in, for example,

dx.doi.org/10.1021/cm302468b | *Chem. Mater.* 2012, 24, 4192−4200

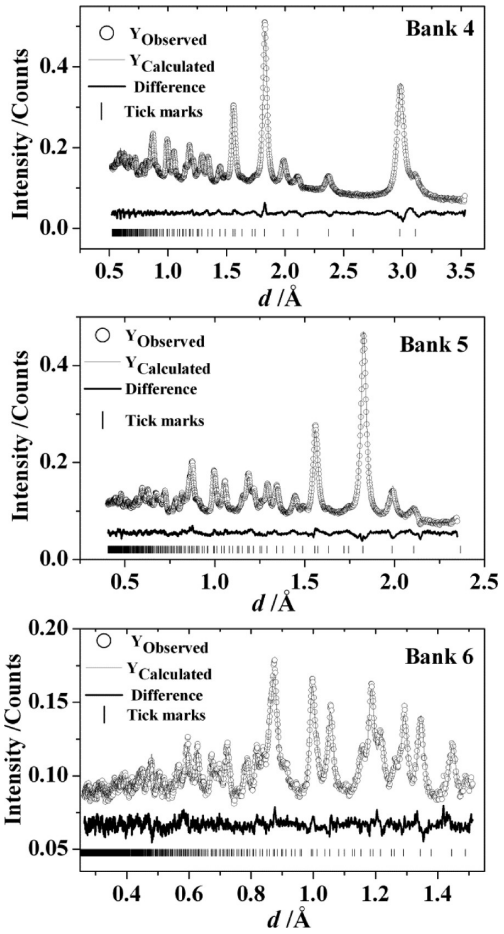

Figure 2. Rietveld fits to neutron powder diffraction data of $Bi_2Ir_2O_7$ by simultaneous analysis of three banks of data from the GEM diffractometer. Refined structural parameters are contained in Table 1.

cerium zirconate pyrochlore:[28] this gave significantly poorer fits to the observed diffraction data. Partial replacement of oxide in the pyrochlore lattice by water or hydroxide ions was ruled out by the lack of any characteristic infrared bands due to these species in the solids, and the lack of any noticeable background of incoherent scattering in the neutron diffraction pattern.

Some other bismuth iridate pyrochlores have already been reported in the literature. A stoichiometric phase $Bi_2Ir_2O_7$ was first reported by Bouchard and Gillson in 1971, but only its lattice parameter was refined (a = 10.3269(2) Å) from powder XRD data.[29] Later, Kennedy studied an oxide-ion deficient phase $Bi_{1.912}Ir_2O_{6.815}$ that had been prepared from the individual oxides by high-temperature annealing and refined its structure from powder neutron diffraction data in the standard pyrochlore space group $Fd\bar{3}m$ with a = 10.3256(1) Å.[30] Koga et al. prepared bismuth iridate pyrochlores by coprecipitation of an amorphous precursor from H_2IrCl_6 and Bi^{3+}, followed by firing to induce crystallinity, but presented no structure refinement of the materials.[31] Most recently, Cosio-Castaneda studied the series $Bi_{2-y}Sr_yIr_2O_7$ and refined the y = 0 end member as a stoichiometric pyrochlore with a = 10.3121 (3) Å.[32] Our refined lattice parameter of 10.32074(31) Å and the refined x coordinate of the 48f oxygen, match closely the refined values of Kennedy's deficient phase, suggesting a similar coordination environment for the metals, despite the fact that our material does not show the same bismuth and oxide deficiency. Our refined Ir−O bond distance of 1.98712(4) Å is entirely consistent with the presence of Ir(IV) and bond valence sums give a value of iridium oxidation state of +4.3.[33]

Figure 3 shows XANES data recorded from the smallest particle size sample of $Bi_2Ir_2O_7$ at the Bi L_{III} edge, along with

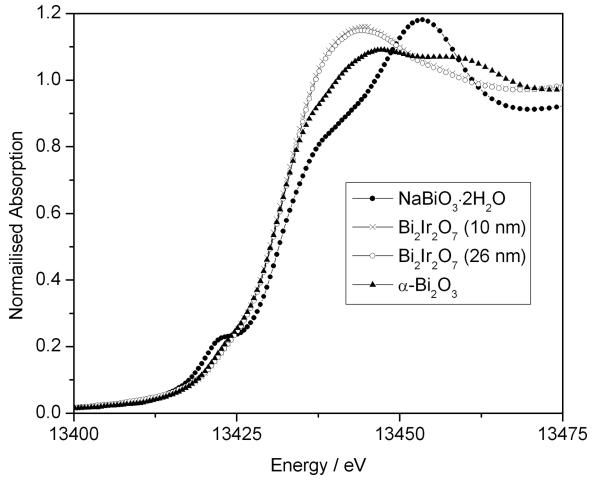

Figure 3. Bi L_{III}-edge XANES data from $Bi_2Ir_2O_7$ and reference materials.

reference materials containing bismuth in known oxidation state. Since we used a Bi(V)-containing precursor in the synthesis of the material, it was important to determine the oxidation state of bismuth in the product, and the XANES spectra clearly show that bismuth is present solely as Bi(III) in the pyrochlore phase: the edge shift matches that of α-Bi_2O_3 and the pre-edge $2p^{3/2}$−6s peak, characteristic of Bi(V),[34] as in $NaBiO_3{\cdot}2H_2O$, is absent. This is consistent with the structure analysis described above, with no evidence for any Bi(V), as seen on the B-site in, for example, bismuth ruthenate pyrochlores.[35]

Figure 4a shows Ir L_{III}-edge XANES spectra along with various reference materials, including some mixed-valent iridium phases that we have recently reported.[17] It has previously been demonstrated that analysis of the Ir L_{III}-edge for oxidation state determination requires calculation of the second derivative spectrum,[36] which is shown for our materials

Table 1. Structural and Thermal Parameters for $Bi_2Ir_2O_7$ Derived from Rietveld Refinement of Neutron Diffraction Data[a]

atom	site	x/a	y/a	z/a	occupancy	U_{11} (× 100 Å^2)	U_{22} (× 100 Å^2)	U_{33} (× 100 Å^2)	U_{12} (× 100 Å^2)	U_{13} (× 100 Å^2)	U_{23} (× 100 Å^2)
Bi1	16d	0.5	0.5	0.5	1	1.48(4)	1.48(4)	1.48(4)	−0.12(7)	−0.12(7)	−0.12(7)
Ir1	16c	0	0	0	1	−0.258 (7)	−0.258 (7)	−0.258 (7)	0.091 (33)	0.091(33)	0.091(33)
O1	48f	0.32629(13)	0.125	0.125	1	0.40 (6)	0.48 (4)	0.48 (4)	0.00	0.00	0.46 (5)
O2	8b	0.375	0.375	0.375	1	2.27 (13)	2.27 (13)	2.27 (13)	0.0	0.0	0.0

[a] $Fd\bar{3}m$ a = 10.32074(31) Å. R_p = 0.0269, R_{wp} = 0.0230 χ^2 = 2.486. The site occupancies were fixed after initial analysis (see text).

dx.doi.org/10.1021/cm302468b | Chem. Mater. 2012, 24, 4192−4200

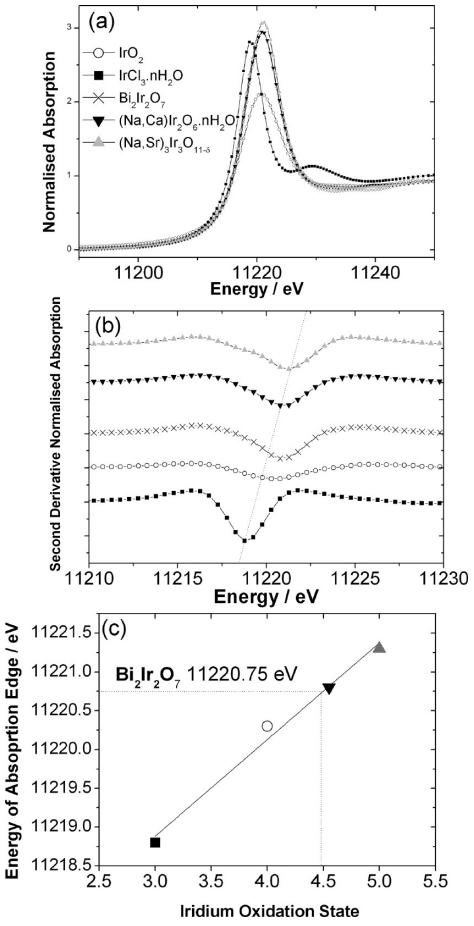

Figure 4. Ir L_{III}-edge XANES data from $Bi_2Ir_2O_7$ and reference materials (a) normalized XANES spectra (b) second derivative curves, and (c) plot of edge position versus oxidation state for the reference materials with the edge position of $Bi_2Ir_2O_7$ indicated. In panel (b), the dotted line indicates the shift in minimum of the second derivative with iridium oxidation state. The reference materials $IrCl_3{\cdot}5H_2O$, IrO_2, $(Na,Ca)_2Ir_2O_6{\cdot}nH_2O$ and $(Na,Sr)_3Ir_3O_{11-\delta}$ have oxidation states of +3, +4, +4.6, and +5, respectively, and in panels (b) and (c), the same symbols from (a) are used to denote each reference material.

in Figure 4b. Figure 4c shows the edge position (the minimum of the second derivative spectrum) as a function of oxidation state for the reference materials with the edge position for $Bi_2Ir_2O_7$ indicated. This graph would suggest that, in $Bi_2Ir_2O_7$, the average oxidation state of iridium is slightly higher than +4, approaching +4.5. To reconcile this result with the result of the neutron structure refinement, which showed Ir−O bond distances characteristic of Ir(IV) and no evidence for inclusion of extra oxide ions, we propose that the high surface area of the ∼10 nm crystallites gives a detectable amount of surface-oxidized iridium. Indeed, we already have shown that, under hydrothermal conditions, in the presence of oxidizing agents, iridium(V) oxides may be formed.[17] We may conclude that the initial Ir(III) present in the reagent $IrCl_3{\cdot}5H_2O$ is oxidized under hydrothermal conditions in the presence of oxidizing species, in the present case, both $NaBiO_3{\cdot}2H_2O$ and Na_2O_2, with an excess of these being needed to avoid decomposition to metallic iridium. The fact that iridium is oxidized to little over +4 (on average) under mild hydrothermal conditions is consistent with studies of the synthesis of iridates under conventional high-temperature reactions, where high oxygen partial pressure,[36] or molten hydroxide fluxes[37] are required to reach higher oxidation states such as Ir(VI). $NaBiO_3{\cdot}2H_2O$ is known to reduce readily under hydrothermal conditions;[38] hence, the formation of Bi(III) in $Bi_2Ir_2O_7$ is not unexpected.

As an additional assignment of metal oxidation states, we measured XPS spectra (see Figure 5). Figure 5a shows the Ir 4*f*

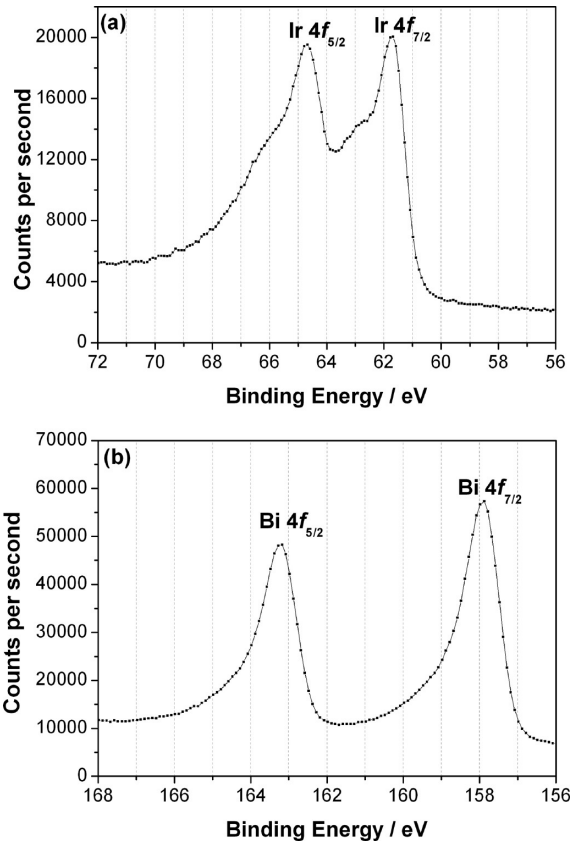

Figure 5. XPS spectra measured in (a) the Ir 4*f* region and (b) the Bi 4*f* region.

region. The $4f_{7/2}$ peak shows a major feature at ∼61.7 eV and a smaller component at ∼62.6 eV. The former would be consistent with the presence of Ir(IV), as in IrO_2 (reported at the same energy for single-crystal IrO_2[39]), while the higher-energy feature would indicate the presence of some iridium oxidized beyond +4. In fact, the spectrum resembles closely that reported by Kennedy for his oxygen-deficient bismuth iridate pyrochlore phase,[30] who found a major peak at 60.86 eV in the $4f_{7/2}$ region, and a higher energy feature at 62.5 eV. Kennedy proposed that surface Ir(V) may therefore be present; this gives further weight to our hypothesis of some surface-oxidized iridium in the hydrothermally prepared sample. Figure 5b shows the Bi 4*f* region. The $4f_{7/2}$ peak essentially shows a broad single feature at 157.9 eV, which is close to the value tabulated for Bi_2O_3 (159.5 eV), suggesting only Bi(III) is present in the material. The slight asymmetry of the peak, which is much less pronounced than in the Ir 4*f* region, is most probably due to the conducting nature of the sample (see below).

Figure 6 shows magnetization data recorded for $Bi_2Ir_2O_7$. The variation of magnetic susceptibility with temperature (see Figure 6a) shows typical paramagnetic behavior in the temperature range of 2−300 K. No noticeable magnetic anomaly or magnetic ordering is observed down to 2 K. The susceptibility is almost temperature-independent with a value of 3.9×10^{-4} emu mol^{-1} at room temperature, which is consistent

dx.doi.org/10.1021/cm302468b | *Chem. Mater.* 2012, 24, 4192−4200

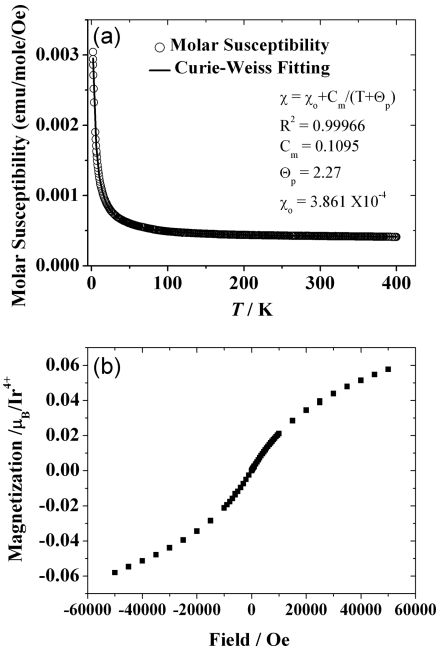

Figure 6. Magnetization measurements from $Bi_2Ir_2O_7$ (a) molar susceptibility versus temperature at H = 10000 Oe with the results of a Curie–Weiss fit and (b) magnetization as a function of field at 2 K. Both measurements were made from the sample made up of 10 nm crystallites: data from the larger crystallites were virtually identical.

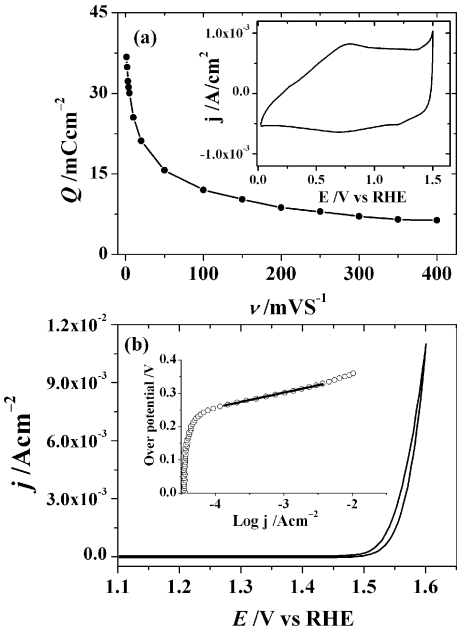

Figure 8. (a) Integrated charge (between 0.3–1.0 V) obtained from voltammogram of $Bi_2Ir_2O_7$ as a function of sweep rate: the inset shows typical voltammogram recorded with a sweep rate of 20 mV s^{-1} (b) Current–voltage plot for oxygen evolution reaction recorded with a sweep rate of 1 mV s^{-1}, inset shows variation of overpotential with current density and liner fitting to the Tafel equation.

with a report for $Bi_2Ir_2O_7$ prepared by solid-state synthesis.[29] The M–H curve at 2 K (see Figure 6b) also exhibits a paramagnetic response; however, the behavior cannot be fitted to a simple Brillouin function. The magnetic data are consistent with other iridium-containing pyrochlores and is believed to be both due to high spin–orbit coupling and a delocalization of d-electrons; indicating that the material is metallic in nature.

The room-temperature resistivity of the hydrothermal $Bi_2Ir_2O_7$ is of the order of 10^{-3} Ω cm, which is similar to that reported for polycrystalline $Bi_2Ir_2O_7$ samples synthesized using solid-state routes.[29,40] The resistivity shows only a small temperature dependence from room temperature down to 2 K (Figure 7), but its overall decrease confirms the metallic nature of the material.

The electrochemical properties of $Bi_2Ir_2O_7$ were examined using the sample with a surface area of 46 m^2 g^{-1} (crystallite size ~10 nm). A typical voltammogram (inset in Figure 8a) showed a broad peak at ~0.8 V and a weak peak at ~1.4 V. Both of these peaks appear quasi-reversible and can be assigned to surface redox processes of Ir sites, as suggested for IrO_2

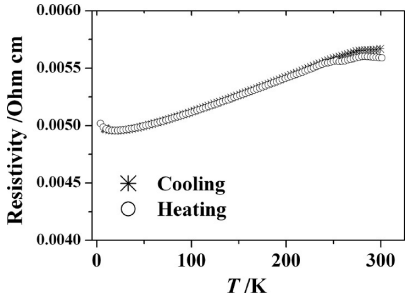

Figure 7. Resistivity versus temperature for 10-nm-particle-size $Bi_2Ir_2O_7$.

electrodes.[41] The effect of sweep rate on the voltammetry was evaluated and used to determine both the outer and total voltammetric charge (Figure 8a).[42] The outer charge represents easily accessible electroactive sites and was estimated by extrapolating the charge at infinite sweep rate; in contrast, the total charge represents all electroactive sites and was estimated by extrapolating the charge at zero sweep rate.[42] This analysis of the $Bi_2Ir_2O_7$ voltammograms gave values of 26 and 58 mC cm^{-2}, for outer (q_O^*) and total (q_T^*) charge, respectively. These values compare favorably with published data for RuO_2–IrO_2 materials studied for OER in acid solutions: for example, Mattos-Costa et al. found q_T^* = 52 mC cm^{-2} for a sample of $50RuO_2$–$50IrO_2$ prepared by annealing an acetonylacetonate sol precursor at 400 °C.[15] The ratio q_I^*/q_T^* (where $q_I^* = q_T^* - q_O^*$, and is the inner charge) gives information about the surface morphology of the electrode[43] and for $Bi_2Ir_2O_7$, this value (0.55) is somewhat higher than that for electrodes prepared from RuO_2 solid solutions (typically 0.2[43,44]): this indicates the presence of porosity in the deposited layer, as would be expected for a material with a relatively high surface area. The activity for the oxygen evolution reaction (OER) of the $Bi_2Ir_2O_7$ layer was evaluated using slow sweep voltammetry in 1 M H_2SO_4 at 25 °C. The onset of activity was found to be 1.45 V vs RHE (Figure 8b) and showed a Tafel slope of 45 mV $decade^{-1}$. Extrapolation of this slope to the equilibrium potential gave an exchange current density (i_0) of 1.76 × 10^{-10} A cm^{-2} geometric. A Tafel slope of 45 mV dec^{-1} can be compared to values reported for similar materials. Values of *ca* 60 mV $decade^{-1}$ have been reported for IrO_2 in acidic electrolytes with lower values being reported for mixed oxides.[6,7,45] In particular, Tunold et al. investigated pure IrO_2 and mixed oxides of Ir with Ru, Sn, and Ta for oxygen evolution activity and found that Ir-rich materials gave Tafel slopes of 30–40 mV $decade^{-1}$.[2] A Tafel slope of 40 mV

dx.doi.org/10.1021/cm302468b | *Chem. Mater.* 2012, 24, 4192–4200

decade^{-1} indicates an *electrochemical oxide* mechanistic pathway, where the rate-determining step involves an electrochemical oxidation of a surface metal site.[2] Therefore, given that $Bi_2Ir_2O_7$ shows a slope of 45 mV decade^{-1}, the oxygen evolution activity is linked to a surface redox process, presumably the one observed at 1.45 V. Interestingly, this potential of OER onset is very similar to values reported for RuO_2−IrO_2 materials in the literature.[7]

As was mentioned in the Introduction, there is little consensus on the mechanism of oxygen evolution catalysis on oxides.[3,6,10−12] Given that the bulk crystal structures are different, it is certainly the case that the surface chemistries of the widely studied rutile-type RuO_2 and IrO_2 materials are different for the pyrochlore material that we have studied here and, indeed, other pyrochlores reported in the literature for OER. Therefore, making direct comparisons in terms of electrocatalysis mechanism is challenging. It is also possible that OER under acidic and basic conditions may proceed via different mechanisms, although, for many materials, activity is observed in both pH regimes.[3] For the rutile-type materials, it is established that RuO_2 has high activity for OER in aqueous acid but is unstable due to irreversible oxidation to water-soluble RuO_4. In contrast, IrO_2 shows less activity: hence, a solid solution of the two oxides represents a compromise to balance activity and stability (at least in the short term, since prolonged use can lead to segregation to give Ir-rich surfaces and a loss of activity).[7] In terms of reactivity, we can compare our Tafel slope value with those for RuO_2−IrO_2 materials, which, as noted above, for the optimal materials that contain mixtures of ruthenium and iridium, are lowered from the value for pure IrO_2 from 60 mV decade^{-1} to 30−40 mV decade^{-1} for OER in acid solution.[2] Since the Tafel slope is a probe of surface reaction mechanism,[3] electrodes fabricated from our $Bi_2Ir_2O_7$ (Tafel slope = 45 mV decade^{-1}) are likely to show similar mechanisms of OER.

The stability of our sample of $Bi_2Ir_2O_7$ in OER was assessed using repetitive potential cycling experiments between 0.02 V and 1.5 V vs RHE at a sweep rate of 50 mV s^{-1}. Figure 9a shows the oxygen evolution current up to 1.5 V after every 100 cycles. Reasonable stability of the OER was found with a loss of only 16% of activity between initial and after 1000 cycles. It is likely that much of this decrease in activity is due to physical loss of material from the electrode, because of bubble formation rather than chemical degradation. The electrochemical stability of the material was confirmed by only minor changes in the voltammetric profile between cycle 1 and cycle 1000 (Figure 9b). In order to assess the stability of the material further, we made studies of a sample that had been immersed in 1.0 M H_2SO_4 acid and held at 95 °C for 24 h. TEM analysis of the sample after this treatment (Figure 10a) shows little change in the overall morphology and size distribution of the crystallites, with particles up to 10 nm diameter being seen. Ir L_{III}-edge XANES of the acid-treated sample (see Figure 10a) shows that the average oxidation state of iridium is unaffected by acid treatment. Furthermore, the bulk metal ratios by ICP analysis is unchanged and ICP analysis of the electrolyte solution after use shows negligible amounts of iridium in solution. These results all corroborate the robust nature of the $Bi_2Ir_2O_7$ electrodes. This may be contrasted with highly active RuO_2 electrodes for OER, which suffer from low stability, with losses of ruthenium into solution occurring readily.[3] In terms of stability, it is also useful to draw comparison with the $Bi_2Ru_2O_{7-y}$ system, whose electrochemical stability was studied by Gökağaç and Kennedy

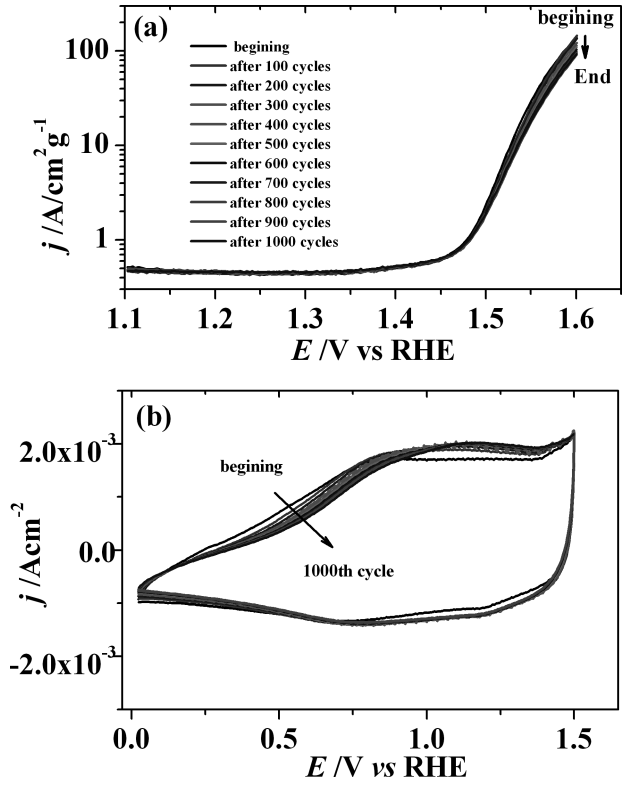

Figure 9. Effect of repetitive potential cycling on the OER of $Bi_2Ir_2O_7$: (a) forward scan of a voltammogram recorded at a sweep rate of 1 mV s^{-1} after every 100 cycles and (b) cyclic voltammogram at 50 mV s^{-1} between 0.02 V and 1.5 V.

in acid solutions.[46] They found that the material showed a high stability toward segregation after long periods of polarization, which they ascribed to a low level of oxygen defects by comparison to related compositions where higher concentrations of defects gave phase separation, yielding bismuth metal, and presumably dissolution of the ruthenium. Thus, the high stability of $Bi_2Ir_2O_7$ electrode would be consistent with this model and the structure analysis presented above, which shows a close to stoichiometric pyrochlore with few oxygen defects.

$Bi_2Ir_2O_7$ has previously been reported to be active for OER under alkaline conditions.[13] ten Kortenaar et al. reported the OER activity of 12 Ir-containing mixed oxides, including pyrochlores and perovskite materials.[13] $Bi_2Ir_2O_7$ was made using a solid-state route in that work and was found to be moderately active for OER but with a much lower i_0 value, relative to that found by us (1.9×10^{-12} A cm^{-2}). This may partially be explained by the low surface area of the sample prepared by the solid-state method and the higher Tafel slope observed (57 mV decade^{-1}). However, a much higher electrode loading of $Bi_2Ir_2O_7$ was used (7 mg cm^{-2} vs 0.4 mg cm^{-2}) in their studies, which would tend to negate these factors. Therefore, we suggest that $Bi_2Ir_2O_7$ is more active under acidic conditions in OER than under alkaline conditions. Interestingly, Beck et al. studied $Bi_2Ir_2O_7$ for ORR activity in 0.5 M aqueous H_2SO_4 and found no activity unless the material was doped with Pt at the B-site.[47]

■ CONCLUSIONS

Hydrothermal synthesis allows the low-temperature (240 °C) formation of the stoichiometric pyrochlore $Bi_2Ir_2O_7$ in one step

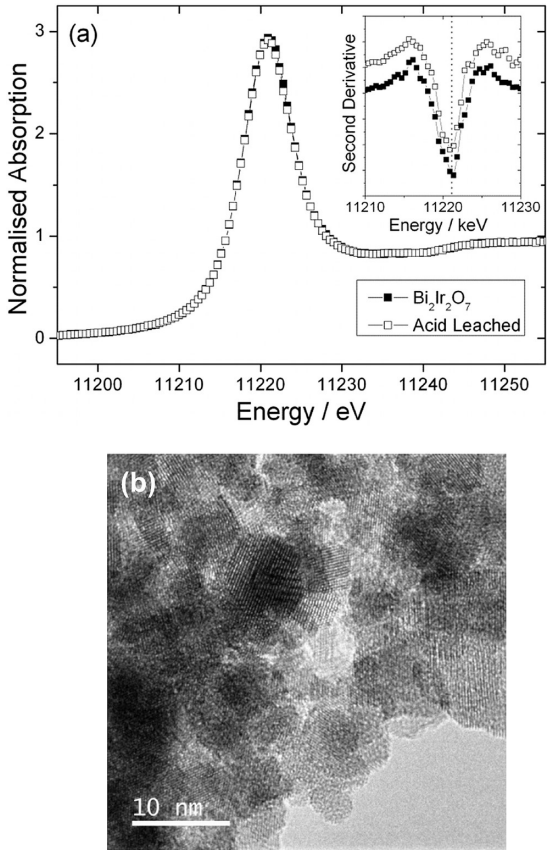

Figure 10. (a) Ir L_{III}-edge XANES spectra of the same $Bi_2Ir_2O_7$ sample (prepared in 5 M NaOH) before and after acid treatment (1 M H_2SO_4 at 95 °C), with the second derivative spectrum given in the inset, and (b) TEM image of sample of $Bi_2Ir_2O_7$ after acid treatment.

from solution. X-ray absorption near-edge structure (XANES) and X-ray photoelectron spectroscopy (XPS) measurements of the samples show some evidence of surface oxidation of iridium, which may be ascribed to the small crystallite size. The material has magnetic and electrical characteristics that match materials of similar composition previously prepared by solid-state synthesis. The material shows good activity and high stability for oxygen evolution in dilute acid electrolyte and analysis of the Tafel slope would suggest that the OER activity is mediated by surface redox processes, similar to that observed in the most active IrO_2–RuO_2 materials. Our work thus shows how the fine powders of hydrothermal $Bi_2Ir_2O_7$ allow the fabrication of robust electrocatalyst electrodes, complementing previous studies of related pyrochlore iridate materials in the oxygen reduction reaction. The pyrochlore contains a lower mole percentage of precious metal than the rutile materials commonly used, so it may present economic benefits in its application. In terms of stability, $Bi_2Ir_2O_7$ appears to present advantages over conventional IrO_2–RuO_2 materials, which are known to suffer from segregation of the elements during prolonged electrochemical use.

AUTHOR INFORMATION

Corresponding Author

*E-mail: r.i.walton@warwick.ac.uk.

Notes

The authors declare no competing financial interest.

ACKNOWLEDGMENTS

We thank the EPRSC (Project Nos. EP/F012721 and EP/H500308) and Johnson Matthey plc for funding this work. We are grateful to Enrico Pettruco (Johnson Matthey) for his valuable discussions during the course of the work described. Some of the equipment used in materials characterization at the University of Warwick was obtained through the Science City Advanced Materials project "Creating and Characterising Next Generation Advanced Materials" with support from Advantage West Midlands (AWM) and partially funded by the European Regional Development Fund (ERDF). We are grateful to the STFC for provision of beamtime at ISIS and to Dr. Ron Smith for his assistance in measuring the powder neutron diffraction data. We thank Diamond Light Source for provision of XAFS beamtime and Dr. Silvia Ramos for her help with measuring data on the B18 beamline.

REFERENCES

(1) Kinoshita, K. *Electrochemical Oxygen Technology*; John Wiley & Sons: New York, 1992.
(2) Tunold, R.; Marshall, A.; Rasten, E.; Tsypkin, M.; Owe, L.-E.; Sunde, S. *ECS Trans.* **2010**, *25*, 102.
(3) Trasatti, S. *Electrochim. Acta* **1984**, *29*, 1503.
(4) Di Blasi, A.; D'Urso, C.; Baglio, V.; Antonucci, V.; Arico, A. S.; Ornelas, R.; Matteucci, F.; Orozco, G.; Beltran, D.; Meas, Y.; Arriaga, L. G. *J. Appl. Electrochem.* **2009**, *39*, 191.
(5) (a) Lyons, M. E. G.; Brandon, M. P. *J. Electroanal. Chem.* **2010**, *641*, 119. (b) Michas, A.; Andolfatto, F.; Lyons, M. E. G.; Durand, R. *Key Eng. Mater.* **1992**, *535*, 72. (c) Takasu, Y.; Yoshinaga, N.; Sugimoto, W. *Electrochem. Commun.* **2008**, *10*, 668.
(6) Lyons, M. E. G.; Floquet, S. *Phys. Chem. Chem. Phys.* **2011**, *13*, 5314.
(7) Owe, L. E.; Tsypkin, M.; Wallwork, K. S.; Haverkamp, R. G.; Sunde, S. *Electrochim. Acta* **2012**, *70*, 158.
(8) (a) Rolewicz, J.; Comninellis, C.; Plattner, E.; Hinden, J. *Electrochim. Acta* **1988**, *33*, 573. (b) Vercesi, G. P.; Salamin, J. Y.; Comninellis, C. *Electrochim. Acta* **1991**, *36*, 991. (c) Hu, J. M.; Zhang, J. Q.; Cao, C. N. *Int. J. Hydrogen Energy* **2004**, *29*, 791.
(9) Murakami, Y.; Tsuchiya, S.; Yahikozawa, K.; Takasu, Y. *Electrochim. Acta* **1994**, *39*, 651.
(10) Vante, N. A.; Schubert, B.; Tributsch, H.; Perrin, A. *J. Catal.* **1988**, *112*, 384.
(11) Shukla, A. K.; Kannan, A. M.; Hegde, M. S.; Gopalakrishnan, J. *J. Power Sources* **1991**, *35*, 163.
(12) Goodenough, J. B.; Manoharan, R.; Paranthaman, M. *J. Am. Chem. Soc.* **1990**, *112*, 2076.
(13) ten Kortenaar, M. V.; Vente, J. F.; Ijdo, D. J. W.; Müller, S.; Kötz, R. *J. Power Sources* **1995**, *56*, 51.
(14) Nakagawa, T.; Bjorge, N. S.; Murray, R. W. *J. Am. Chem. Soc.* **2009**, *131*, 15578.
(15) Mattos-Costa, F. I.; de Lima-Neto, P.; Machado, S. S.; Avaca, L. A. *Electrochim. Acta* **1998**, *44*, 1515.
(16) (a) Modeshia, D. R.; Walton, R. I. *Chem. Soc. Rev.* **2010**, *39*, 4303. (b) Riman, R. E.; Suchanek, W. L.; Lencka, M. M. *Ann. Chim.* **2002**, *27*, 15. (c) Demazeau, G. *J. Mater. Chem.* **1999**, *9*, 15. (d) Feng, S. H.; Xu, R. R. *Acc. Chem. Res.* **2001**, *34*, 239.
(17) Sardar, K.; Fisher, J.; Thompsett, D.; Lees, M. R.; Clarkson, G. J.; Sloan, J.; Kashtiban, R. J.; Walton, R. I. *Chem. Sci.* **2011**, *2*, 1573.
(18) Darton, R. J.; Turner, S. S.; Sloan, J.; Lees, M. R.; Walton, R. I. *Cryst. Growth Des.* **2010**, *10*, 3819.
(19) Sardar, K.; Playford, H. Y.; Darton, R. J.; Barney, E. R.; Hannon, A. C.; Tompsett, D.; Fisher, J.; Kashtiban, R. J.; Sloan, J.; Ramos, S.; Cibin, G.; Walton, R. I. *Chem. Mater.* **2010**, *22*, 6191.
(20) Smirnova, O.; Azuma, M.; Kumada, N.; Kusano, Y.; Matsuda, M.; Shimakawa, Y.; Takei, T.; Yonesaki, Y.; Kinomura, N. *J. Am. Chem. Soc.* **2009**, *131*, 8313.

(21) (a) Williams, W. G.; Ibberson, R. M.; Day, P.; Enderby, J. E. *Physica B* **1998**, *241−243*, 234. (b) Hannon, A. C. *Nucl. Instrum. Methods A* **2005**, *551*, 88.
(22) Larson, A. C.; Dreele, R. B. V. Technical Report LAUR 86-748, Los Alamos National Laboratory, Albuquerque, NM, 1994.
(23) Toby, B. H. *J. Appl. Crystallogr.* **2001**, *34*, 210.
(24) Dent, A. J.; Cibin, G.; Ramos, S.; Smith, A. D.; Scott, S. M.; Varandas, L.; Pearson, M. R.; Krumpa, N. A.; Jones, C. P.; Robbins, P. E. In *14th International Conference on X-Ray Absorption Fine Structure*; DiCicco, A., Filipponi, A., Eds.; Iop Publishing, Ltd.: Bristol, U.K., 2009; Vol. *190*.
(25) Ravel, B.; Newville, M. *J. Synchrot. Radiat.* **2005**, *12*, 537.
(26) Subramanian, M. A.; Aravamudan, G.; Rao, G. V. S. *Prog. Solid State Chem.* **1983**, *15*, 55.
(27) Ismunandar; Kennedy, B. J.; Hunter, B. A. *Mater. Res. Bull.* **1999**, *34*, 1263.
(28) Thomson, J. B.; Armstrong, A. R.; Bruce, P. G. *Chem. Commun.* **1996**, 1165.
(29) Bouchard, R. J.; Gillson, J. L. *Mater. Res. Bull.* **1971**, *6*, 669.
(30) Kennedy, B. J. *J. Solid State Chem.* **1996**, *123*, 14.
(31) Koga, K.; Momai, T.; Matsunaga, M. *ECS Trans.* **2008**, *11*, 101.
(32) Cosio-Castaneda, C.; de la Mora, P.; Tavizon, G. *J. Solid State Chem.* **2011**, *184*, 1251.
(33) Wills, A. S. *Valist*: deposited at www.ccp14.dl.ac.uk, 1999.
(34) Jiang, N.; Spence, J. C. H. *J. Phys.-Condens. Matter* **2006**, *18*, 8029.
(35) Horowitz, H. S.; Longo, J. M.; Lewandowski, J. T. *Mater. Res. Bull.* **1981**, *16*, 489.
(36) (a) Choy, J. H.; Kim, D. K.; Demazeau, G.; Jung, D. Y. *J. Phys. Chem.* **1994**, *98*, 6258. (b) Choy, J. H.; Kim, D. K.; Hwang, S. H.; Demazeau, G.; Jung, D. Y. *J. Am. Chem. Soc.* **1995**, *117*, 8557.
(37) Mugavero, S. J.; Smith, M. D.; Yoon, W. S.; zur Loye, H. C. *Angew. Chem., Int. Ed.* **2009**, *48*, 215.
(38) Kinomura, N.; Kumada, N. *Mater. Res. Bull.* **1995**, *30*, 129.
(39) Chen, R. S.; Huang, Y. S.; Liang, Y. M.; Tsai, D. S.; Chi, Y.; Kai, J. J. *J. Mater. Chem.* **2003**, *13*, 2525.
(40) Beck, E.; Kemmlersack, S. *J. Less Common Met.* **1987**, *135*, 257.
(41) Ardizzone, S.; Carugati, A.; Trasatti, S. *J. Electroanal. Chem.* **1981**, *126*, 287.
(42) Ardizzone, S.; Fregonara, G.; Trasatti, S. *Electrochim. Acta* **1990**, *35*, 263.
(43) Gaudet, J.; Tavares, A. C.; Trasatti, S.; Guay, D. *Chem. Mater.* **2005**, *17*, 1570.
(44) Cheng, J. B.; Zhang, H. M.; Chen, G. B.; Zhang, Y. N. *Electrochim. Acta* **2009**, *54*, 6250.
(45) (a) de Oliveira-Sousa, A.; da Silva, M. A. S.; Machado, S. A. S.; Avaca, L. A.; de Lima Neto, P. *Electrochim. Acta* **2000**, *45*, 4467. (b) Matos-Costa, F. I.; Lima Neto, P. d.; Machado, S. A. S.; Avaca, L. A. *Electrochim. Acta* **1998**, *44*, 1515. (c) Marshall, A. T.; Haverkamp, R. G. *Electrochim. Acta* **2010**, *55*, 1978. (d) Alves, V. A.; da Silva, L. A.; Boodts, J. F. C.; Trasatti, S. *Electrochim. Acta* **1994**, *39*, 1585.
(46) Gökağaç, G.; Kennedy, B. J. *J. Electroanal. Chem.* **1994**, *368*, 235.
(47) Beck, N. K.; Steiger, B.; Scherer, G. G.; Wokaun, A. *Fuel Cells* **2006**, *6*, 26.